

# Genetically programmable optical random neural networks

Bora Çarpınlioğlu, Bahrem Serhat Daniş, Uğur Teğın\*

Department of Electrical and Electronics Engineering, Koç University, Istanbul, 34450, Türkiye

\*utegin@ku.edu.tr

## Abstract

Today, machine learning tools, particularly artificial neural networks, have become crucial for diverse applications. However, current digital computing tools to train and deploy artificial neural networks often struggle with massive data sizes and high power consumptions. Optical computing provides inherent parallelism and perform fundamental operations with passive optical components. However, most of the optical computing platforms suffer from relatively low accuracies for machine learning tasks due to fixed connections while avoiding complex and sensitive techniques. Here, we demonstrate a genetically programmable yet simple optical neural network to achieve high performances with optical random projection. By genetically programming the orientation of the scattering medium which acts as a random projection kernel and only using 1% of the search space, our novel technique finds an optimum kernel and improves its initial test accuracies 7-22% for various machine learning tasks. Our optical computing method presents a promising approach to achieve high performance in optical neural networks with a simple and scalable design.

## Introduction

Nowadays, artificial neural networks are heavily used for learning from data to perform intricate tasks of high complexity<sup>1</sup>. In the last decade, machine learning applications started to cover diverse fields, from autonomous driving to healthcare diagnosis, and demonstrate outstanding success in real-life applications<sup>2</sup>. With the availability of high volumes of data, the trend of machine learning is to develop computationally complex and data-hungry giant models. This increasing complexity in machine learning models adds computational and environmental challenges during training and inference steps<sup>3</sup>. Moreover, the currently used digital computing platforms, which are based on Turing–von Neumann architecture, are notoriously limited by the memory access bottleneck and cannot keep up with the demands of large models efficiently. The current transistor-based computing methods are reaching the physical and technological limits, indicating the end of Moore's Law.

Since all the information in the world is natively analog, analog computing is an intuitive alternative hardware solution for creating and deploying machine learning models. Unlike digital computing, which processes information in discrete values (0s and 1s), analog computing operates on continuous signals; thus, it is compatible with complex,

high-dimensional data. However, analog computing is intrinsically noisy and not as precise as digital computing. The neural networks' relative robustness against noise and device imperfections makes them ideal applications for analog computing solutions. In recent decades, analog computing tools such as brain-inspired (neuromorphic) computing methods, including approaches like reservoir computing<sup>4</sup> and extreme learning machines<sup>5,6</sup>, emerged. With fixed connections in the reservoir or hidden layers, these methods provide decent accuracy with less training effort.

Optical computing, a brunch of analog computing, serves as a prominent candidate to accelerate machine learning efforts by offering several key operations like Fourier transform, convolution operations, and matrix multiplications intrinsically<sup>7</sup>. This rich framework has led to the development of optical computers capable of pattern recognition<sup>8</sup> and the optical implementation of neural network models<sup>9</sup> rapidly. However, initial efforts faced challenges in controlling/training optical connections and implementing nonlinear connections. With the introduction of neuromorphic computing methods in the 2000s, the training problem of optical computing has been circumvented. Recently, interest in optical neural networks has grown with free space, fiber, and integrated designs<sup>10-12</sup>. In its simple form, implementing artificial neural networks efficiently and rapidly in optics can be achieved by utilizing optical diffraction, wave propagation, and passive optical elements like lenses and/or scattering media<sup>13,14</sup>. Especially, using a disordered medium comprising millions of fully connected photonic nodes serves as a static random reservoir<sup>15</sup> with random matrix multiplication and offers random mapping of data for dimensionality reduction<sup>16</sup>. By incorporating digital feedback loops to the fixed random mapping of a disordered medium, optical neural networks are demonstrated for chaotic system prediction<sup>17,18</sup>.

Here, we present the first genetically programmable optical random neural network and improve the performance of scattering-based optical computing platforms for machine learning applications. Our novel method is based on finding an optimum random projection kernel to map information optically for designated machine learning applications by altering the disordered medium (diffuser) orientation inside the optical neural network. We employ an evolutionary search algorithm (genetic algorithm) and significantly increase accuracy for various datasets by using only 1% of the search space to find optimum random projection kernels. Our simple programmable optical neural network has been tested on binary and multilabel classification tasks using Breast MNIST<sup>19</sup>, Covid-19 X-Ray<sup>20</sup>, and Fashion MNIST<sup>21</sup> datasets. Test accuracies are improved from 70% to 77%, 78% to 93%, and 58% to 80%, respectively.

## Results

Experimental realization of our genetically programmable optical random neural network is illustrated in Fig. 1. It consists of a continuous-wave (CW) laser source, a spatial light modulator (SLM), a pair of lenses to perform Fourier transforms, a scattering medium placed on a disc located on the Fourier plane to provide optical random projection and a camera to collect optically processed information. The optical

information encoding process is carried out by superimposing each sample of the dataset, an 8-bit image, as a phase pattern on the SLM.

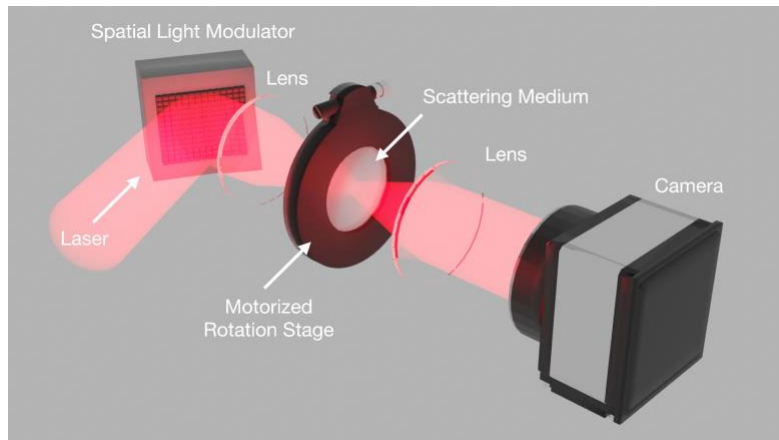


**Figure 1:** Schematic of random projection-based programmable optical computing setup. the experimental setup consists of a spatial light modulator for encoding information onto laser light, a scattering medium on off-axis rotation stage, and an imaging system to relay light and a camera to decode information.

After the encoding step, the information-carrying optical field is processed linearly all the way up until the camera. Optical random projection/mapping is realized with a diffuser. Here the optical neural network leverages Johnson-Lindenstrauss Lemma<sup>22</sup>. It states that random projection can be used for dimensionality reduction purposes<sup>23</sup>, which is at the core of learning from high-dimensional data.

When coherent light passes through the diffuser, different optical free paths are formed at different points on the scattering media, and at the camera plane, we obtain a speckle pattern. A small change in the orientation of the diffuser changes the result of the element-wise matrix multiplication, i.e., the convolution kernel is dependent on the orientation of the diffusing medium. Therefore, we propose searching for and finding an optimum kernel (diffuser surface) with better feature extraction capabilities. Since the information-carrying laser beam occupies a small region on the diffuser, introducing a new region to it by rotating the diffuser changes the random projection kernel. For this purpose, we constructed a disk covered with adhesive tape, which resulted in a search space where there is only one degree of freedom (angular position), allowing us to search for better kernels easily.

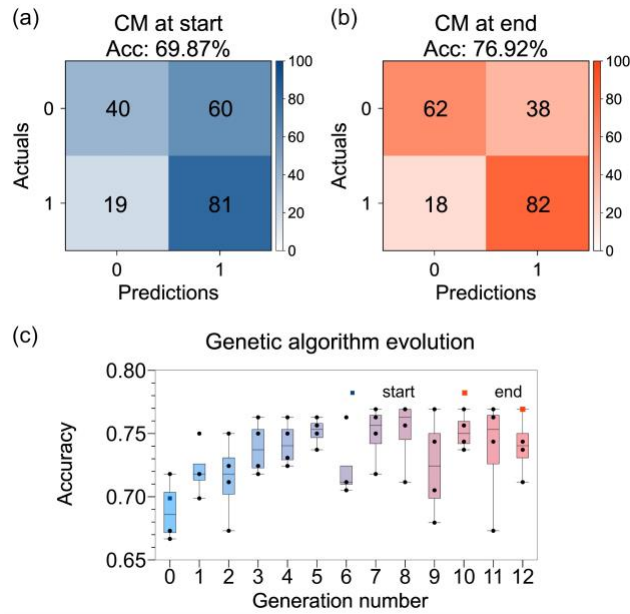


**Figure 2:** Experimental learning results for the Breast MNIST dataset. **a,b** Confusion matrices (CM's) corresponding to the first and the last genetic algorithm (GA) iteration. **c** Evolution of the accuracy during GA.

A stepper motor is employed to control the orientation of the diffuser with the half-stepping method, where one full rotation of the disk is divided into 4096 steps. Without benefitting optimization algorithms and trying each possible kernel individually, evaluating the resulting accuracy would take a long time experimentally. Thus, we utilize a heuristic search algorithm, genetic algorithm (GA)<sup>24</sup>, for optimizing for the maximum accuracy, which is a function of the angular position,  $\theta$ . Such a method requires several trials to meet the designated task and decreases optimization time in experiments. The deployment of a heuristic search algorithm like GA can also be attributed to the uneven structure of the complex media, where there is no a priori relationship between the complex random matrices obtained from distinct points significantly far from each other. However, we want to emphasize that since the rotation steps are small, similarities in output images correspond to matrices originating from a neighborhood of consecutive angular positions are observed in our experiments (see Supplementary Information for quantitative metrics). GA parameters used in this study can be found in Supplementary Information and the backend processing steps are explained in Methods.

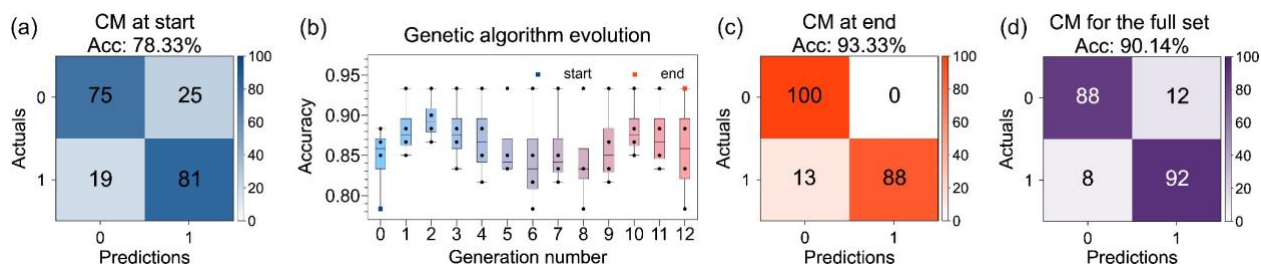


**Figure 3:** Experimental learning results for the COVID-19 X-Ray dataset when a subset of the full dataset is used for GA. **a** Confusion matrix (CM) corresponding to the first genetic algorithm (GA) iteration. **b** Evolution of the accuracy during GA. **c** CM obtained at the end of GA. **d** CM corresponding to the full dataset when all the samples are passed through the optimal angular position yielded by GA.

We initially employ GA on a binary classification task to test our genetically programmable optical neural network. Using the Breast MNIST<sup>19</sup> dataset containing 780 samples, we achieve the GA evolution plot presented in Fig. 2c. We first perform ridge regression to samples without processing optically to determine the baseline performance and find the accuracy to be 66.67%. After the first iteration in GA, a ridge classification accuracy of 69.87% is reported, which is already above the baseline performance. Based on these classification accuracies in the following iterations, GA proposes an optimal point where the ridge classification accuracy reached its maximum, 76.92%. We present the improvement in classification accuracy by plotting confusion matrices at the beginning (Fig. 2a) and the end (Fig. 2b) of the programming process. The confusion matrices are normalized such that entries on the same row sum up to 100, barring rounding errors. These confusion matrices for the Breast MNIST dataset demonstrate that classification performance can be significantly improved by programming the optical computing platform and searching for an optimal random projection kernel.

Encouraged by the results in binary classification accuracy, we decided to scale up and tackle a more complex dataset, the COVID-19 X-Ray<sup>20</sup> containing 2481 samples. However, the SLM used in this study operates at a 60 Hz repetition rate since liquid crystal technology is limited in terms of speed. To decrease the time spent on the programming of the random projection kernel and make our optical computing method useful for larger datasets, we propose to form a smaller subset of the dataset to be considered a proxy to the full set for the programming step. For this purpose, a subset of size 300 containing randomly selected 150 positive and 150 negative samples is created and we run GA with the same parameters. This way, our goal is to reduce the programming time while maintaining the improvements in classification accuracy. As demonstrated in Fig. 3b, we observe a significant increase in the ridge classification accuracy from 78.33% to 93.33% while programming the optical computing platform with GA.

To evaluate our method of programming the optical computing platform with a subset of the dataset, we optically process all the samples of the COVID-19 dataset with the optimized random projection kernel proposed by GA. An accuracy of 90.14% is achieved over the baseline accuracy level of the dataset, which is 75.45%. These results demonstrate that the genetically programmed optical computing platform provides 15% higher accuracy. To determine the disadvantage of utilizing a subset for programming the optical computing platform, we applied GA on the entire dataset, using all 2481 samples instead of 300 samples, and observed a maximum accuracy level of 91.15%. It shows that by utilizing a randomly selected subset and decreasing the programming time significantly, we sacrifice a 1% performance difference in classification, and even a small subset gives rise to improvements in classification accuracy. We can observe the evolution of accuracy via the confusion matrices presented in Fig. 3 and c. The confusion matrix corresponding to the entire dataset is also given in Fig. 3d.

To increase the complexity of the task and evaluate our method's performance with large datasets, we study the Fashion MNIST dataset with 70,000 samples<sup>21</sup>. Similar to the COVID-19 X-Ray dataset, we utilize the generating of a subset to decrease the programming time of our optical neural network. Thus, a subset of randomly selected 3000 samples is created from 70,000 samples of the Fashion MNIST dataset. To set a baseline for our method, we apply the ridge classification over the selected subset and obtain 73.83% accuracy. At the beginning of the programming, after the first GA iteration, an accuracy of 58.17% is obtained. At the end of the programming, this classification accuracy is increased to 80.17% (Fig. 4b), resulting in a 23% improvement. The entire Fashion MNIST dataset is optically processed for the programmed condition, and the classification accuracy of 81.88% is achieved. The row-wise normalized confusion matrices captured during the evolution of GA (Fig. 4a, c) and inference (Fig. 4d) further supported our claim that programming random neural networks effectively decrease classification errors.

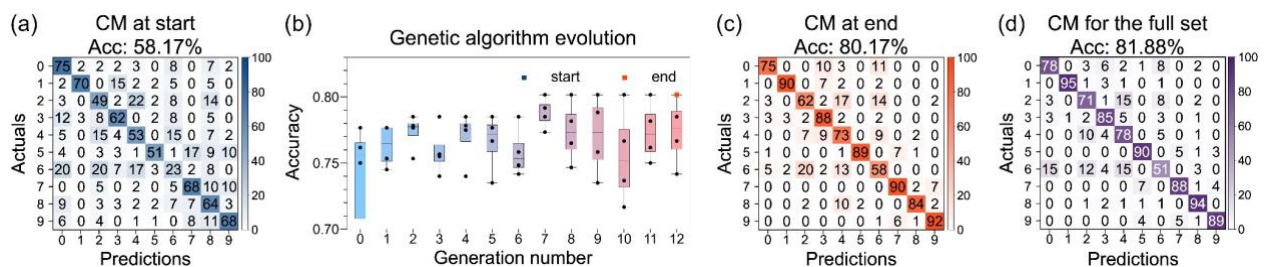


**Figure 4:** Experimental learning results for the Fashion MNIST dataset when a subset of the full dataset is used for GA. **a** Confusion matrix (CM) corresponding to the first genetic algorithm (GA) iteration. **b** Evolution of the accuracy during GA. **c** CM obtained at the end of GA. **d** CM corresponding to the full dataset when all the samples are passed through the optimal angular position yielded by GA.

## Discussion



To understand the effect of the programming random projection kernel with a genetic algorithm, we perform linear discriminant analysis (LDA), a dimensionality reduction technique, on the Fashion MNIST dataset. LDA helps us to illustrate the inner workings of our optical computing platform. In Fig. 5, 960 features obtained from the randomly mapped subset of the dataset were represented by three components. The distribution of color-coded classes shows that the clustering performance of optical random projection improves as GA progresses. The clustering of similar samples eases the task of the readout layer, thus increasing the performance of the optical computing method.

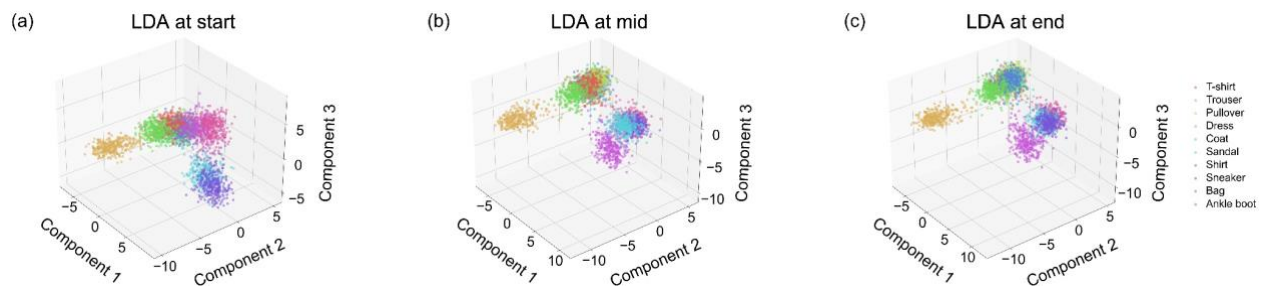


Figure 5: LDA performed on a subset of the Fashion MNIST dataset (a) before GA, (b) for an arbitrary iteration of GA, and (c) after GA has found the optimal random projection kernel.

Without sacrificing the simplicity of the demonstrated optical computing platform, a nonlinear activation function such as the inverse rectified linear unit (ReLU) function can be implemented by partially saturating the measured beam profiles via either increasing the laser power or tuning the camera parameters. In the literature, the effect of such an additional nonlinearity has been reported<sup>25</sup>. It can increase the accuracy of the machine learning tasks when incorporated with the absolute square measurement introduced by the intensity detection of the camera at the readout layer.

In our study, the preferred camera can record 8-bit grayscale images. However, we emulate a camera capable of representing images using fewer bits to test our approach in data-scarce settings by mapping the range 0-255 to a smaller range. We observe that with such a device, faster data rates would be enabled without sacrificing the classification accuracy (see Fig. S6 and Table S1 in Supplementary Information). We conclude that with suitable hardware tailored for modern machine vision tasks requiring real-time performance, our programmable reservoir can continue to perform machine learning tasks with high accuracy.

The presented programmable optical computing platform can be further improved with alternative programming algorithms. For example, one can use surrogate optimization tools<sup>26</sup> instead of GA, choose a different/learnable weighting parameter  $\alpha$  in Eq. 4 during ridge classification, or change the pool size used in local averaging, which would affect the number of features pertaining to each captured image. Although we have yet to opt to make these changes for the sake of simplicity and not losing the essence of our endeavor, they can potentially increase the ridge classification accuracy of the readout layer.

Energy consumption in our setup is only due to the power requirements of components such as the laser source, SLM, and camera. All processing, including the random matrix multiplication, is done passively and our computing platform relies on linear optics. It indicates that the consumed energy is independent of the sample resolution. Our work opens up an avenue for energy-efficient optical processing schemes based on reservoir computing ideas to be engineered for success in modern machine learning practice.

## Methods

### Physical model of genetically programmable optical random neural network.

Here  $A(x, y)$  and  $\phi(x, y)$  represent the amplitude and the phase of the incoming laser beam and  $S(x, y)$  denotes a sample of a dataset. With the help of an SLM, they create the following expression,

$$O(x, y) = A(x, y) \exp [j\phi(x, y)] \exp [jS(x, y)] \quad (1)$$

for the laser beam with the encoded information,  $O(x, y)$ . The mathematical expression which indicates the operation of the optical random neural network can be shown as

$$R(x, y) = F^{-1}\{F\{O(x, y)\}H(f_x, f_y; \theta)\} \quad (2)$$

$$I(x, y) = |R(x, y)|^2 \quad (3)$$

where  $H(f_x, f_y; \theta)$  is the complex, random matrix representing the diffuser (its transfer matrix) as parameterized by the angular position of the disk,  $\theta$ ,  $R(x, y)$  is the received optical field at the camera plane, and  $I(x, y)$  its intensity recorded by the camera. Here,  $x$  and  $y$  denote spatial coordinates while  $f_x$  and  $f_y$  denote spatial frequency coordinates.

The classification operation performed by the readout layer can be expressed as

$$w^* = \operatorname{argmin}_w |y - Xw|^2 + \alpha|w|^2 \quad (4)$$

where the optimum weights  $w^*$  are inferred from a training set with images  $X$  and corresponding labels  $y$ .  $\alpha$  governs the regularization strength, which is set to 1 throughout all experiments.

**Experimental procedure.** A continuous-wave laser source with a central wavelength of 1064 nm is used for illuminating a spatial light modulator (SLM, HAMAMATSU X10468) with 800 x 600 pixels resolution. Since the samples we used originate from datasets developed for machine learning tasks, they typically have low resolution e.g., 28 x 28 pixels. To be able to maximally use the effective area of our SLM, we performed image upsampling by an integer factor. The phase encoding process was then carried out as shown by the expressions above.



We placed an adhesive tape at the processing plane as the scattering medium providing random matrix multiplication. The scattering medium was rotated to different angles using a stepper motor (28BYJ-48) to yield parameterizations of the random matrix. Since the classification accuracies depend on the random matrix values, and no a priori relationship is known among different random matrix distributions corresponding to different angles, a heuristic search algorithm, genetic algorithm (GA)<sup>24</sup>, was utilized for optimizing for the maximum accuracy.

While programming the optical random neural network, at each GA iteration, all the dataset samples are optically processed with a particular candidate random projection kernel and collected with the camera. All camera parameters, including exposure, saturation, and gain, are kept constant throughout the experiment. Captured 2D RGB images are converted to grayscale images and downsampled by local averaging with a pool size of (20,16) (see Supplementary Information for the selection of the pool size). As a final step, downsampled 2D grayscale images are converted to 1D arrays (flattened), and ridge classification is performed. The fitness function in GA is set as the classification accuracy, and depending on the result, the stepper motor is rotated to the angle yielded by GA. Following this pipeline, GA searches and finds the kernel that provides the best accuracy level for designated datasets.

### **Funding**

This work is supported by the Scientific and Technological Research Council of Turkey (TÜBİTAK) under grant number 123E308.

### **Acknowledgements**

We thank Aydoğın Özcan for fruitful discussions and Çağrı Şenel for providing the SLM and laser source used in experiments.

### **Data availability statement**

Data and code related to the results in this work may be obtained from the authors upon reasonable request.

### **Conflicts of interest**

The authors declare no conflicts of interest.

**Supplementary information** The online version contains supplementary material available at ...

### **References**

1. Haykin, S. S. *Neural networks and learning machines*. (Pearson Education, 2009).
2. Esteva, A. *et al.* A guide to deep learning in healthcare. *Nat. Med.* **25**, 24–29 (2019).
3. Schmidhuber, J. Deep learning in neural networks: An overview. *Neural Netw.* **61**, 85–117

- (2015).
4. Tanaka, G. *et al.* Recent advances in physical reservoir computing: A review. *Neural Netw.* **115**, 100–123 (2019).
  5. Huang, G.-B., Zhu, Q.-Y. & Siew, C.-K. Extreme learning machine: theory and applications. *Neurocomputing* **70**, 489–501 (2006).
  6. Kesgin, B. U. & Teğın, U. Machine Learning with Chaotic Strange Attractors. (2023).
  7. Goodman, J. W. *Introduction to Fourier optics*. (Roberts and Company publishers, 2005).
  8. Abu-Mostafa, Y. S. & Psaltis, D. Optical Neural Computers. *Sci. Am.* **256**, 88–95 (1987).
  9. Farhat, N. H., Psaltis, D., Prata, A. & Paek, E. Optical implementation of the Hopfield model. *Appl Opt* **24**, 1469–1475 (1985).
  10. Wetzstein, G. *et al.* Inference in artificial intelligence with deep optics and photonics. *Nature* **588**, 39–47 (2020).
  11. Shen, Y. *et al.* Deep learning with coherent nanophotonic circuits. *Nat. Photonics* **11**, 441–446 (2017).
  12. Teğın, U., Yıldırım, M., Oğuz, İlker, Moser, C. & Psaltis, D. Scalable optical learning operator. *Nat. Comput. Sci.* **1**, 542–549 (2021).
  13. Lin, X. *et al.* All-optical machine learning using diffractive deep neural networks. *Science* **361**, 1004–1008 (2018).
  14. Pierangeli, D. *et al.* Living optical random neural network with three dimensional tumor spheroids for cancer morphodynamics. *Commun. Phys.* **3**, 160 (2020).
  15. Saade, A. *et al.* Random Projections through Multiple Optical Scattering: Approximating Kernels at the Speed of Light. in *2016 IEEE International Conference on Acoustics, Speech and Signal Processing (ICASSP)* 6215–6219 (IEEE Press, 2016). doi:10.1109/ICASSP.2016.7472872.
  16. Gigan, S. Imaging and computing with disorder. *Nat. Phys.* **18**, 980–985 (2022).
  17. Dong, J., Rafayelyan, M., Krzakala, F. & Gigan, S. Optical reservoir computing using multiple light scattering for chaotic systems prediction. *IEEE J. Sel. Top. Quantum Electron.* **26**, 1–12 (2019).

18. Rafayelyan, M., Dong, J., Tan, Y., Krzakala, F. & Gigan, S. Large-Scale Optical Reservoir Computing for Spatiotemporal Chaotic Systems Prediction. *Phys Rev X* **10**, 041037 (2020).
19. Yang, J. *et al.* MedMNIST v2-A large-scale lightweight benchmark for 2D and 3D biomedical image classification. *Sci. Data* **10**, 41 (2023).
20. Soares, E., Angelov, P., Biaso, S., Froes, M. H. & Abe, D. K. SARS-CoV-2 CT-scan dataset: A large dataset of real patients CT scans for SARS-CoV-2 identification. *MedRxiv* 2020–04 (2020).
21. Xiao, H., Rasul, K. & Vollgraf, R. Fashion-MNIST: a Novel Image Dataset for Benchmarking Machine Learning Algorithms. (2017).
22. Johnson, W. B. Extensions of Lipschitz mapping into Hilbert space. in *Conference modern analysis and probability, 1984* 189–206 (1984).
23. Bingham, E. & Mannila, H. Random projection in dimensionality reduction: applications to image and text data. in *Proceedings of the seventh ACM SIGKDD international conference on Knowledge discovery and data mining* 245–250 (2001).
24. Gad, A. F. PyGAD: An Intuitive Genetic Algorithm Python Library. (2021).
25. Pierangeli, D., Marcucci, G. & Conti, C. Photonic extreme learning machine by free-space optical propagation. *Photonics Res.* **9**, 1446–1454 (2021).
26. Eriksson, D., Bindel, D. & Shoemaker, C. A. pySOT and POAP: An event-driven asynchronous framework for surrogate optimization. *ArXiv Prepr. ArXiv190800420* (2019).

# Supplementary information for

## Genetically programmable optical random neural networks

Bora Çarpınlioğlu, Bahrem Serhat Daniş, Uğur Teğın\*

Department of Electrical and Electronics Engineering, Koç University, Istanbul, 34450, Türkiye  
\*uteğın@ku.edu.tr

### Supplementary Discussion 1: 4f Imaging System and Input Encoding

The beam expander with the Keplerian design applied to the laser beam consists of two lenses placed in parallel at a distance equal to the sum of their focal lengths and its magnification can be calculated by the ratio of the focal lengths of the constituent lenses. The lenses used in this 4f imaging system are two bi-convex lenses with focal lengths of 30 mm and 268 mm. In the 4f imaging system, input beam inversion does not pose a problem for us because the output beam has the same intensity pattern as the input due to the azimuthal symmetry of the input Gaussian beam. As a result, SLM receives a magnified laser beam whose input intensity pattern did not change. Similarly, after reflection from the SLM, we use a 4f imaging system, again using two bi-convex lenses with focal lengths of 268 mm and 50 mm.

In the encoding step, since the size of the samples in the datasets was often smaller than the size of the SLM, we performed image upsampling using bilinear interpolation for each sample such that the illuminated region on the SLM was filled with the sample. In areas where the SLM could not be filled by the rescaled image, we simply performed zero-padding.

### Supplementary Discussion 2: Genetic Algorithm Details

Genetic algorithm (GA) employs biology-inspired operations such as mutation, crossover and selection. In order to utilize GA, we formulated a fitness function where higher accuracies were favored, the input parameter being angular position  $\theta$  specified in terms of the steps of the motor in the interval  $[0,4095]$ , and the output being the ridge classification accuracy of the randomly-mapped dataset. We specified 12 generations and a population size of 4 for each generation in GA. In the first generation, all genes were selected randomly, then genes with superior classification accuracies were chosen as mating parent genes (2 in our case) and a new generation was created by mutation (random mutation with 1% probability) and crossover (single-point crossover with 80% probability) operations. We obtained the optimal kernel like so. To ensure a nondecreasing nature for the accuracy, we kept the best gene in a

given generation and passed it onto the next generation. So for each generation, 3 new genes were chosen by GA. In total, the dataset was passed through 40 locations.

To calculate the fitness function corresponding to each gene, we used a laptop with Intel Core i7-7600U CPU and 8 GB RAM that sends commands via serial communication to a microcontroller board (Arduino Uno) which processes step sequences to rotate the stepper motor to the orientation specified by genes.

### Supplementary Discussion 3: Similarity Between Adjoint Random Projection Kernels

To see the similarity between different random projection kernels, we performed two additional experiments. First, we fixed a reference point on our diffuser (disk with the adhesive tape) and rotated it within a range of 9 steps in either direction, which corresponds to an angular span of  $1.58^\circ$ , and recorded the resulting image at each angular position. We hypothesized that, by calculating the similarity between any image and the reference image, we could get a measure of the relation between corresponding random projection kernels. Because of its popularity in image processing and deep learning, we used the structural similarity index measure (SSIM). Fig. S1 shows the average SSIM for five trials. As can be seen in the figure, the general trend manifests itself as a negative correlation between angular displacement (in absolute terms) and similarity.

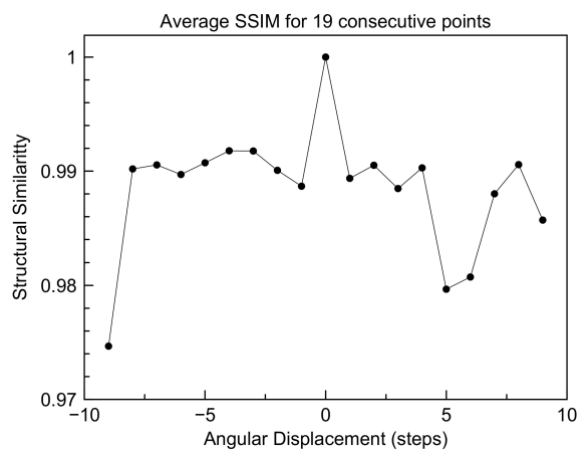


Figure S1: Average SSIM for consecutive points on the diffuser.

Second, we rotated the diffuser for  $0^\circ$ ,  $90^\circ$ ,  $180^\circ$  and  $270^\circ$  while a sample from the Fashion-MNIST dataset is displayed on the SLM. In Fig. S2 we show captured images and normalized average difference images together with SSIM values when the no rotation case is set as a reference.

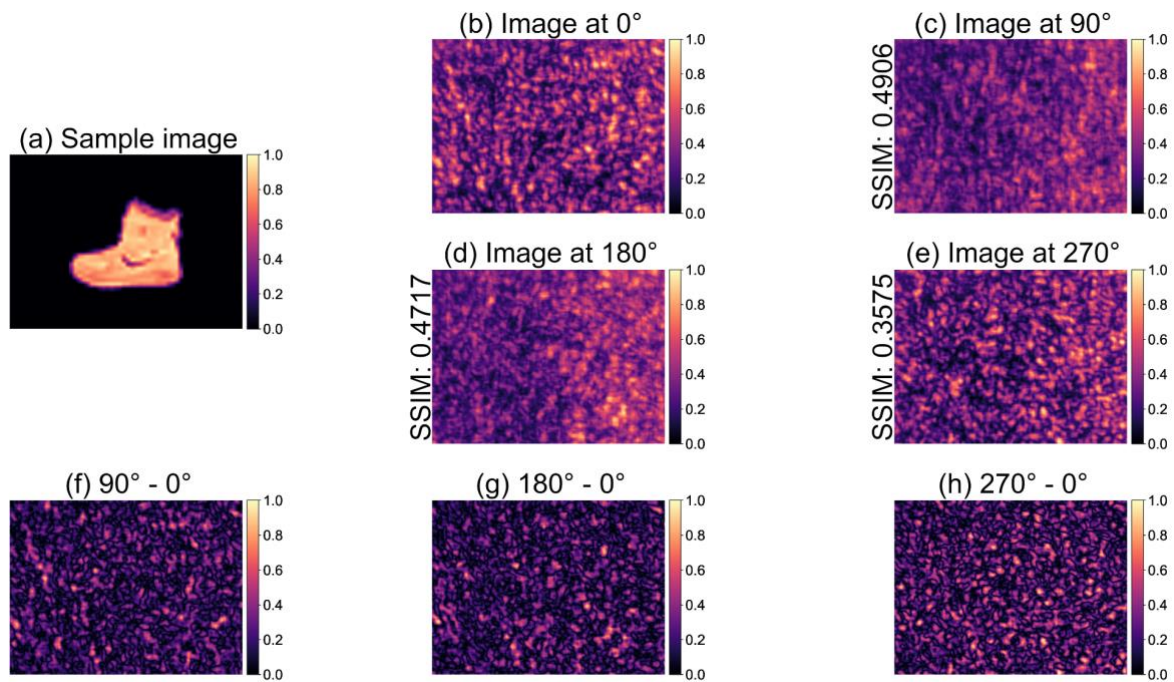


Figure S2: (a) Sample image from the Fashion MNIST dataset. (b-e) Captured images when the diffuser is rotated for  $0^\circ$ ,  $90^\circ$ ,  $180^\circ$  and  $270^\circ$ . SSIM values are given to the left of the images when applicable. (f-h) Difference images when the no rotation case is considered as a reference.

#### Supplementary Discussion 4: Further Results on the Subset Method

As discussed in Main, accuracy results related to the COVID-19 X-Ray dataset were obtained using a subset method. We also performed GA on the full dataset to be able to assess the effectiveness of the subset method i.e., when all 2481 samples are randomly mapped. For the whole dataset, we obtained an accuracy of 91.15% compared to 90.14% obtained from 300 samples, which shows the approximation capability of the subset method. Fig. S3 shows the confusion matrices and the evolution of the accuracy in this setting.



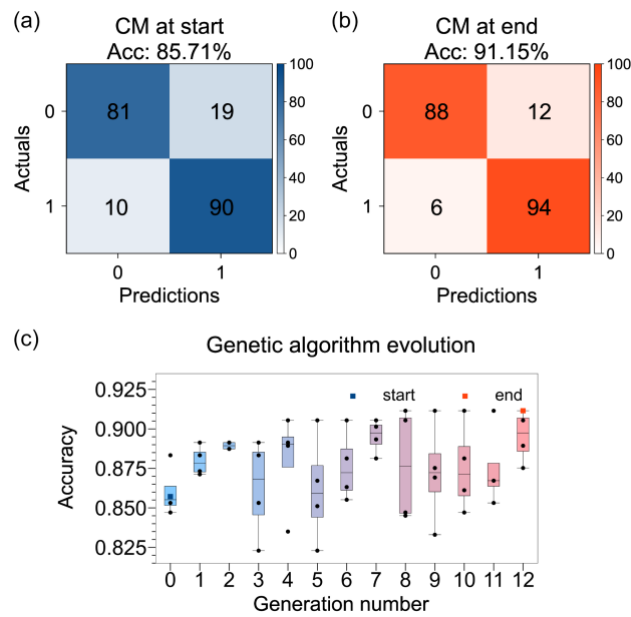


Figure S3: Results for the COVID-19 X-Ray dataset when the full set is used for GA. (a) Confusion matrix corresponding to the first GA iteration. (b) Confusion matrix obtained at the end of GA. (c) Evolution of the accuracy during GA. CM denotes confusion matrix and Acc denotes accuracy.

### Supplementary Discussion 5: Detailed Visualization of Clustering Performance

Fig. S4 shows 3D LDA results on the randomly-mapped subset of the Fashion MNIST dataset for the best GA iteration from various elevation and azimuthal angles.

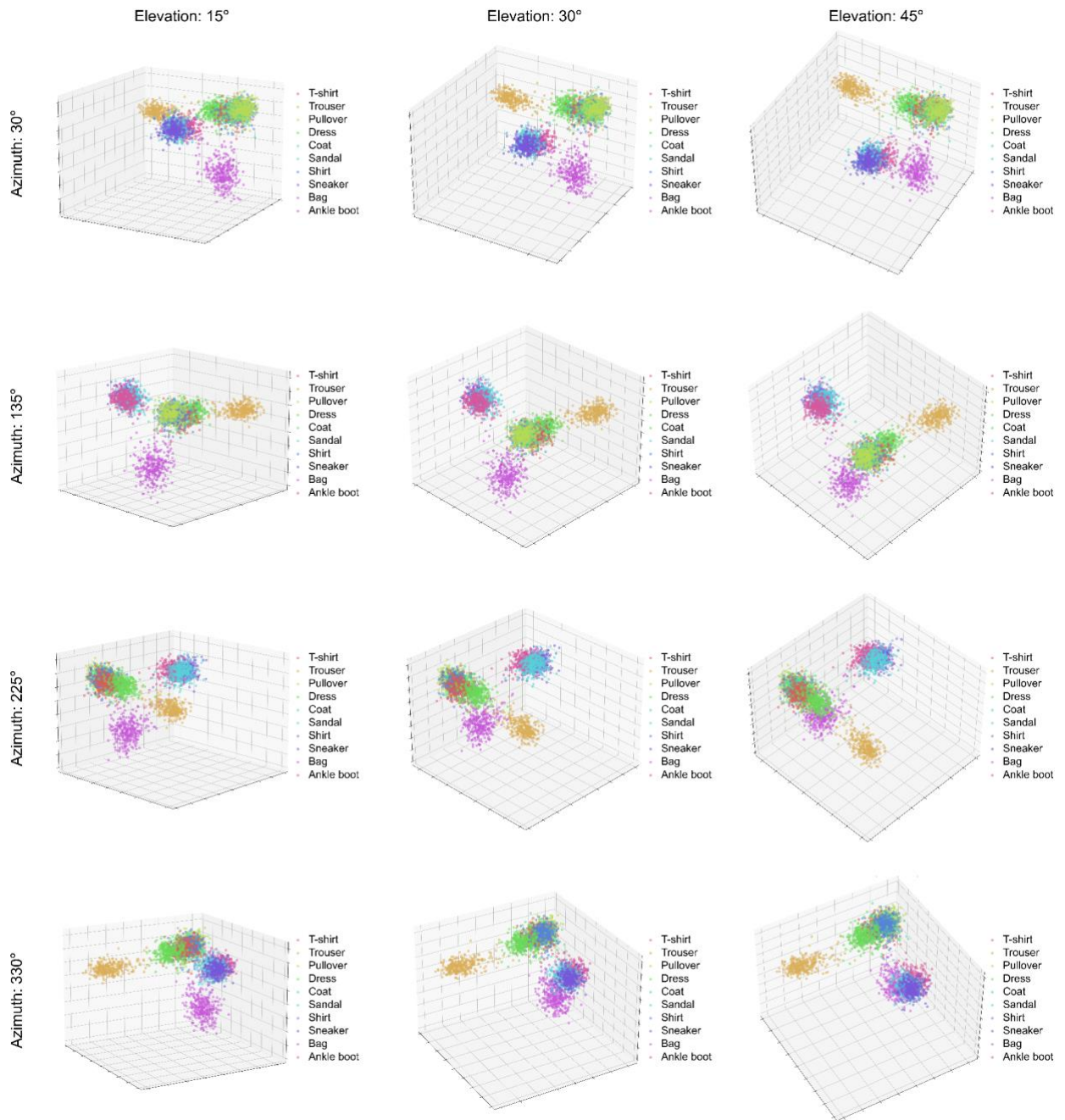


Figure S4: 3D LDA results on the randomly-mapped Fashion MNIST dataset for the best GA iteration for elevation angles of 15°, 30° and 45° and azimuthal angles of 30°, 135°, 225° and 330°.

### Supplementary Discussion 6: Effects of Data Compression on Performance

When applying local averaging to randomly mapped data to reduce the number of pixels used for ridge classification, we fixed a pool size of (20,16). Fig. S5 shows alternative pool sizes and the corresponding number of pixels along with ridge classification accuracies.

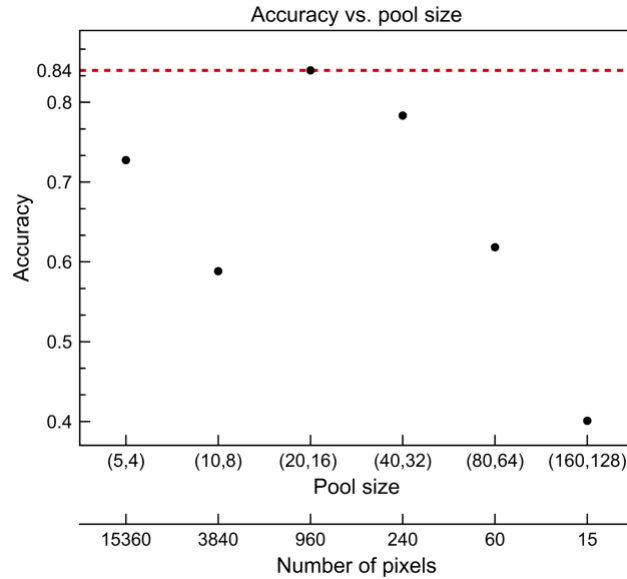


Figure S5: Ridge classification accuracies corresponding to different pool sizes used in local averaging for a randomly mapped subset of the Fashion MNIST dataset consisting of 6000 samples. The maximum accuracy is obtained for the aforementioned pool size of (20,16).

Data compression can also be carried out through reducing the bit depth in captures obtained from randomly mapped inputs. In our experimental setup, we used a camera capable of recording 8-bit grayscale images. Although practically not possible because of the way digital computers process data, we emulated a camera capable of representing images using less bits to test our approach in data-scarce settings by mapping the range 0 – 255 to a smaller range. If such an operation were possible, faster data rates would be enabled without sacrificing the classification accuracy. Fig. S6 shows GA results for different bit depths. We conclude that with suitable hardware tailored for modern machine vision tasks, our method can offer improvements in classification accuracy.

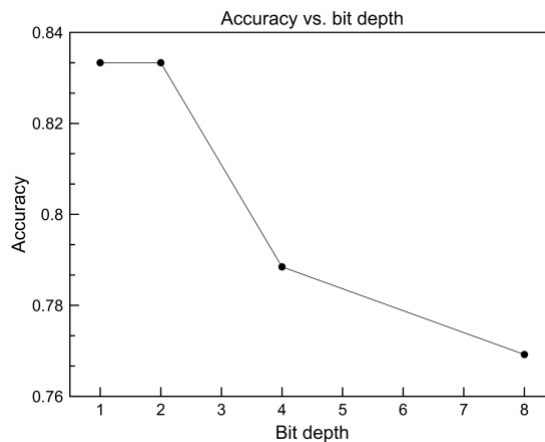


Figure S6: Dependence of ridge classification accuracy on the bit depth of captures in the Breast MNIST dataset. Separate experiments were carried out where 8-bit

original captures were normalized and represented with 1, 2, and 4 bits. A maximum accuracy of 83.33% was obtained for bit depths of 1 and 2.

Table S1 demonstrates the effectiveness of our approach by comparing the classification accuracies obtained by (i) processing the randomly-mapped, 8-bit data and (ii) running GA from scratch (Fig. S6) to yield representations using less bits. These cases are denoted by the “accuracy without GA” and “accuracy with GA” rows, respectively. Without GA, after reducing 8-bit captures to 4-, 2-, and 1-bits and applying pooling and ridge classification, we observed small to no changes in classification accuracies, whereas when we let GA search for the optimal random mapping in different quantization schemes, we observed relatively higher improvements. This implies the adaptive nature of our approach to cases where high bitrates are desired when bit depth can be sacrificed. Modern machine vision tasks requiring real-time performance, therefore, could be a future application where we can test our programmable reservoir.

Table S1: Comparison of different quantization schemes in terms of classification accuracy with and without running GA for the Breast MNIST dataset.

	<b>8-bits</b>	<b>4-bits</b>	<b>2-bits</b>	<b>1-bit</b>
<b>Accuracy without GA</b>	76.92%	76.92%	77.56%	76.28%
<b>Accuracy with GA</b>	-	78.85%	83.33%	83.33%

### Supplementary Discussion 7: Benchmarking Accuracy Levels

To provide a broader perspective, we compared our approach with other popular approaches on the same datasets, taking into account the number of parameters used in each approach. This comparison is presented in Table S2 below. From the table, one can conclude that programmable optical random neural networks generalize well across different datasets when the number of parameters are constrained.

Table S2: Comparison of different approaches in terms of their classification accuracy and number of parameters for different datasets.

<b>Dataset</b>	<b>Approach</b>	<b>Test accuracy</b>	<b>Number of parameters</b>
Breast MNIST	Our approach	76.92%	961
	ResNet-18 <sup>1</sup>	86.3%	~11 million
	Ridge regression	66.67%	784

COVID-19 X-Ray	Our approach	90.14%	961
	ResNet-101 <sup>2</sup>	95.58%	~44.5 million
	Ridge regression	75.45%	160,000
Fashion MNIST	Our approach	81.88%	961
	ResNet-18 <sup>3</sup>	94.9%	~11 million
	Ridge regression	81.13%	784

## References

1. Yang, J. *et al.* MedMNIST v2-A large-scale lightweight benchmark for 2D and 3D biomedical image classification. *Sci. Data* **10**, 41 (2023).
2. Covid-19 Binary Classification | ResNet101 | 96%.
3. GitHub - zalando-research/fashion-mnist: A MNIST-like fashion product database. Benchmark — github.com.